Dynamics of meniscus-bound particle clusters in extensional flow ⓕ✓

Sagar Chaudhary ⓘD ; Sachin S. Velankar ⓘD ; Charles M. Schroeder ✉ ⓘD

Check for updates

View Online

Export Citation

Dynamics of meniscus-bound particle clusters in extensional flow

Sagar Chaudhary,[1,2] Sachin S. Velankar,[3] and Charles M. Schroeder[2,4,5,6,a)]

[1]*Department of Mechanical Science and Engineering, University of Illinois at Urbana-Champaign, Urbana, Illinois 61801*
[2]*Beckman Institute for Advanced Science and Technology, University of Illinois at Urbana-Champaign, Urbana, Illinois 61801*
[3]*Department of Chemical and Petroleum Engineering, University of Pittsburgh, Pittsburgh, Pennsylvania 15260*
[4]*Department of Chemical and Biomolecular Engineering, University of Illinois at Urbana-Champaign, Urbana, Illinois 61801*
[5]*Department of Materials Science and Engineering, University of Illinois at Urbana-Champaign, Urbana, Illinois 61801*
[6]*Center for Biophysics and Quantitative Biology, University of Illinois at Urbana-Champaign, Urbana, Illinois 61801*

Abstract

Capillary suspensions are three-phase mixtures containing a solid particulate phase, a continuous liquid phase, and a second immiscible liquid forming capillary bridges between particles. Capillary suspensions are encountered in a wide array of applications including 3D printing, porous materials, and food formulations, but despite recent progress, the micromechanics of particle clusters in flow is not fully understood. In this work, we study the dynamics of meniscus-bound particle clusters in planar extensional flow using a Stokes trap, which is an automated flow control technique that allows for precise manipulation of freely suspended particles or particle clusters in flow. Focusing on the case of a two-particle doublet, we use a combination of experiments and analytical modeling to understand how particle clusters rearrange, deform, and ultimately break up in extensional flow. The time required for cluster breakup is quantified as a function of capillary number Ca and meniscus volume V. Importantly, a critical capillary number Ca_{crit} for cluster breakup is determined using a combination of experiments and modeling. Cluster relaxation experiments are also performed by deforming particle clusters in flow, followed by flow cessation prior to breakup and observing cluster relaxation dynamics under zero-flow conditions. In all cases, experiments are complemented by an analytical model that accounts for capillary forces, lubrication forces, hydrodynamic drag forces, and hydrodynamic interactions acting on the particles. Results from the analytical models are found to be in good agreement with experiments. Overall, this work provides a new quantitative understanding of the deformation dynamics of capillary clusters in extensional flow.© *2024 Published under an exclusive license by Society of Rheology.* https://doi.org/10.1122/8.0000805

I. INTRODUCTION

Capillary state suspensions are formed by adding a second immiscible liquid to a particle suspension, resulting in the formation of particle clusters bound by liquid capillary bridges [1,2]. Capillary suspensions are a remarkably simple class of materials with tunable properties and are encountered in a wide range of applications such as low fat food formulations, 3D printing, porous ceramics, and conductive pastes for printed electronics [3–10]. In addition, the transition of a mixture from a fluidlike two-phase suspension to a gel-like capillary suspension [2] can be used to overcome issues related to particle sedimentation [11] and to enhance yield stress [1,12]. Despite their importance in industrial applications, mixing operations for preparing capillary suspensions remain largely empirical [13,14]. From this view, we lack a complete understanding of the rheology and fluid mechanics required to control and manipulate the dynamic microstructure of capillary suspensions in flow.

The wetting of solid particles by a second liquid leads to clustering, resulting in the formation of liquid-bound particle clusters that serve as the building blocks of capillary suspensions. Early experimental work focused on measuring the capillary force on particles in the presence of a liquid bridge. MacFarlane and Tabor calculated the force of adhesion due to surface tension between a flat plate and a bead covered in a thin film of liquid for a stationary system [15]. In 1965, Mason and Clark designed a method to measure the forces exerted on two polyethylene hemispheres by liquid bridges of a di-*n*-butyl phthalate/liquid paraffin mixture suspended in water [16]. Mason and Clark used relatively large particles (radius $R = 1.5$ cm) to facilitate facile and accurate experimental measurements because interparticle forces are expected to increase proportionately with particle size. Over the last few decades, improvements in experimental techniques have allowed for more accurate measurements of smaller magnitude capillary forces. Willett *et al.* measured capillary forces using a sensitive microbalance interfaced with a computer, enabling measurement of a wide range of particle radii and bridge volumes [17].

The discussion thus far has been restricted to static forces wherein the particle motion is sufficiently slow to be regarded as quasistatic. Shifting the focus to forces between moving

particles, Pitois *et al.* investigated the effects of meniscus viscosity on capillary and viscous forces for small bridge volumes between two moving spheres [18]. Displacement-controlled experiments were performed where meniscus-bound spheres were mechanically separated until rupture, and the forces were measured as a function of separation distance and sphere velocity. Analytical expressions for capillary and viscous forces were developed and compared with the experiments. Recently, Bozkurt and co-workers studied the effects of wettability and meniscus volume on the capillary force between two equally sized moving glass beads using a similar displacement-controlled approach. Capillary force was measured for various particle radii and separation velocities, and the experimental data were compared with analytical models in the literature [18–20]. Theoretical work on liquid bridges has also been performed to estimate capillary forces. Early work dates back to 1926, when Fisher approximated the shape of the bridge as a toroid [21]. Following this work, Derjaguin used an approximation where the meridian radius of the toroidal shaped bridge is much smaller than the radius of the neck, yielding an analytical expression for the capillary force [22,23]. The Derjaguin equation was subsequently used by several researchers in the field for capillary suspensions [24,25]. However, the toroidal and Derjaguin approaches for calculating capillary forces are only valid for small bridge volumes and small interparticle distances [26], resulting in significant errors at large separations. Motivated by these limitations, several researchers have developed more accurate expressions for the capillary force in liquid bridges [18,24,27].

Broadly, prior work on capillary state suspensions has largely focused on either quasistatic particle clusters or displacement-controlled motion of particles, where the relative motion between particles is prescribed by a mechanical system. However, this experimental scenario is not representative of mixing flows encountered by freely suspended particles in capillary suspensions where the relative motion of particles is dominated by hydrodynamic forces exerted by the surrounding fluid. For these reasons, we lack a complete understanding of the fundamental rheology and fluid mechanics in capillary state suspensions which will help to inform the design of mixing operations in bulk systems. Key questions include: What is the characteristic time scale required for a liquid-bound cluster to rupture in flow? What is the effect of the bridge volume or particle wettability on cluster dynamics and breakup? And what is the role of interparticle hydrodynamic interactions in cluster breakup in flow? Despite recent progress, the dynamics of freely suspended liquid-bound particle clusters in flow is not fully understood.

Unlike particle clusters, flow-induced breakup has been extensively studied for liquid droplets. Research on the breakup dynamics of immiscible liquid droplets traces back to 1934, when G. I. Taylor studied the deformation and bursting of a drop in a second immiscible liquid under various controlled flow conditions, generating extensional flow using a manually controlled "four roller" apparatus and shear flow using a "parallel band" apparatus [28]. Taylor developed criteria for drop deformation as a function of dimensionless flow strength (capillary number, Ca) [28].

Several decades later, Grace investigated droplet breakup in extensional and shear flow, resulting in the classic Grace curve, which plots critical capillary number Ca_{crit} for drop breakup as a function of the viscosity ratio of the suspension [29]. Bentley and Leal used a computer-controlled four-roll mill to study elongation and breakup of small liquid droplets in two-dimensional linear flows [30]. Experiments using the four-roll mill were performed for various flow types, and drop shapes were compared with predictions from several burst theories [30]. Numerical studies on shape relaxation and capillary breakup of initially extended drops under no-flow conditions have also been conducted for various initial drop shapes [31]. Despite the seemingly vast amount of prior literature on liquid drop dynamics, far less insight is available into the micromechanics of meniscus-bound particle clusters. In fact, many of the same physical questions arise for particle clusters bound by liquid bridges; for instance, what is the relaxation behavior of an initially extended cluster? What is the critical capillary number Ca_{crit} required for cluster breakup? And what is the effect of the viscosity of the bridge fluid relative to the bulk fluid? Although these questions have been resolved for liquid droplets decades ago, they have not yet been addressed for meniscus-bound particle clusters in external flows. Recent advances in automated flow control [32–36] provide an ideal approach to study the dynamics of freely suspended particle clusters in precisely controlled flows.

In this work, we investigate the dynamics of meniscus-bound particle doublets (two-particle clusters) in planar extensional flow using a Stokes trap [32], which allows for the manipulation of particles in precisely defined flows. Meniscus-bound particle doublets (clusters with two particles) are the basic unit comprising capillary suspensions. Experiments are complemented by analytical models that incorporate the effects of capillary forces, lubrication forces, hydrodynamic drag forces, and hydrodynamic interactions acting on the particles. Our results show that particle cluster doublets undergo reorientation and eventual breakup in extensional flow above a critical capillary number Ca_{crit}. The analytical model is used to predict Ca_{crit} for cluster breakup as well as to understand the effects of capillary number Ca and meniscus volume V on breakup time. Particle cluster relaxation is further studied under zero-flow conditions revealing insights regarding capillary and viscous modes of relaxation. In all cases, experimental results are in good agreement with the analytical model. Taken together, our results present a fundamental understanding of particle cluster dynamics in external flows that could be useful for designing and implementing mixing processes for capillary suspensions.

II. MATERIALS AND METHODS

A. Microfluidic device and Stokes trap

An automated flow technique known as the Stokes trap [32–34,36] is used to study the dynamics of meniscus-bound particle clusters in flow. We use a four-channel microfluidic device with a cross-slot geometry at the center to generate planar extensional flow (Fig. 1). Using the Stokes trap, meniscus-bound particle clusters are confined near the stagnation
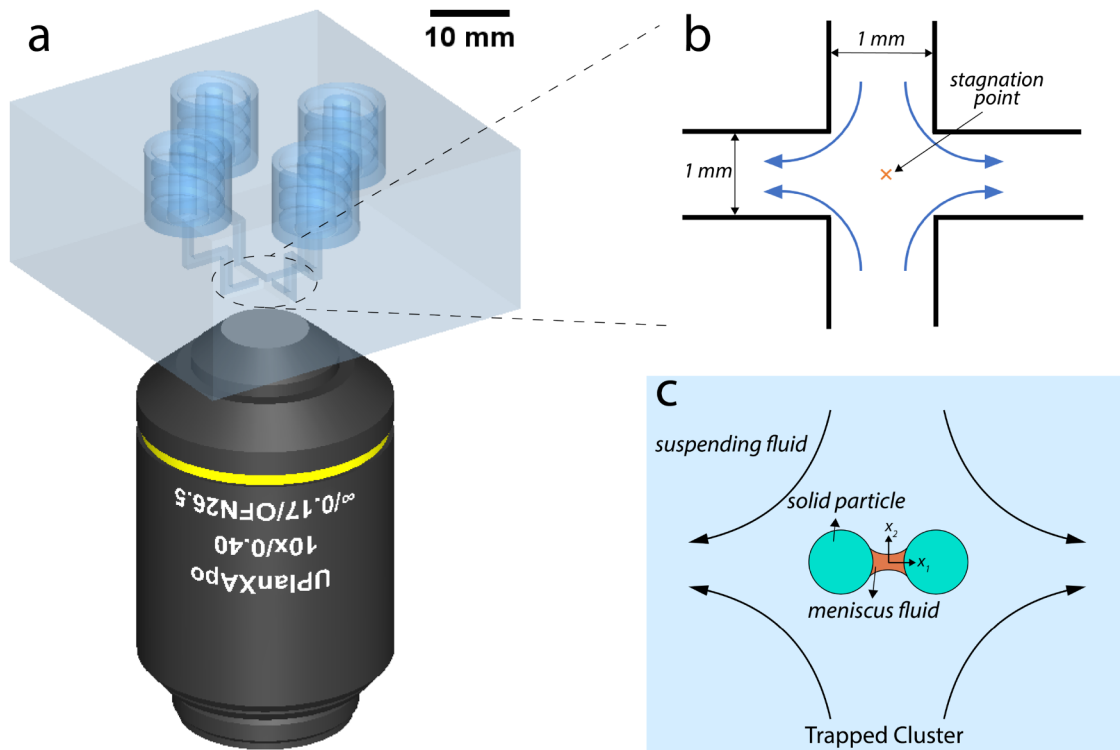
FIG. 1. Schematic of the microfluidic device used to study particle cluster dynamics in extensional flow. (a) Schematic of the four-channel microfluidic device fabricated using SLA 3D printing along with a $10\times$ magnification air-immersion objective lens. The height and width of the channels is 1 mm. The four channels are connected to fluid reservoirs pressurized by regulators and controlled using a LABVIEW program. The cross-slot geometry generates a planar extensional flow, and the open surface of the device is sealed with a glass coverslip for optical microscopy. (b) Schematic showing a zoomed-in view of the four-channel cross-slot in the microfluidic device. The curved arrows depict the extensional flow, and the stagnation point is labeled near the center of the cross-slot. Channel width is 1 mm. (c) Schematic showing a two-particle meniscus-bound cluster trapped in extensional flow at the stagnation point. The suspending fluid, solid particles, and the meniscus fluid are labeled. The radius of the particles is $50\,\mu$m.

point in extensional flow for long times or accumulated fluid strain. The microfluidic device is fabricated using a stereolithography (SLA) 3D printer (Form 3, Formlabs) utilizing a photopolymer clear resin (V4, Formlabs). Devices are printed with 1 mm-wide by 1 mm-tall channel dimensions using a previously reported procedure by Tu *et al.* [36]. The bottom surface of the microdevice is sealed with a glass coverslip to allow for optical microscopy, as previously reported [36]. The Stokes trap is used in conjunction with an inverted microscope (Olympus IX71) coupled with a CMOS camera (Grasshopper 3, FLIR), with the entire setup placed on a vibration-damped optical table (Thorlabs). The microfluidic device is mounted on the microscope stage, and a $10\times$ magnification air-immersion objective lens (0.4 NA, numerical aperture) is used to image into the cross-slot area [Fig. 1(a)], resulting in $0.586\,\mu$m/pixel. The camera captures images at an average rate of 18 frames per second, which varies slightly between experiments, though the exact rate is identified and quantified for each individual particle cluster experiment. All four inlet/outlet channels of the device are connected via polytetrafluoroethylene (PTFE) tubing to fluid reservoirs, three of which contain only the bulk suspending fluid, and the remaining channel contains a low concentration of particle clusters in the bulk suspending fluid. The reservoirs are pressurized using high-precision pressure regulators (Elveflow OB1MK3+) with a pressure stability of 0.005% (0.0014 psi) to establish and control a pressure driven flow in the device. A model

predictive control (MPC) algorithm [32] is used together with a custom LabVIEW interface to control the flow field and manipulate and trap particle clusters near the stagnation point of planar extensional flow in the center of the cross-slot channel.

Numerical simulations of the flow geometry are performed using COMSOL Multiphysics to model the flow of a Newtonian fluid (viscosity 10 Pa s) in a 3D model of the device. Channel dimensions (width and height) are set to 1 mm to match the device dimensions in experiments. Two of the four channels are designated as inlets, and the remaining two channels are assigned as outlets. A no-slip boundary condition is specified for solid surfaces in the entire geometry, and the velocity profile is solved using the Stokes equations, yielding a zero velocity stagnation point at the center of the cross-slot.

B. Materials

Silicone oil (density $\rho_c = 0.971$ g/ml, Sigma-Aldrich) is used as the suspending fluid, polyisobutene (PIB-24, density $\rho_d = 0.89$ g/ml, Soltex) is used as the meniscus fluid, and polyethylene (PE) spheres (100 μm diameter, Cospheric) are used as the solid particulate phase. Particle roughness was determined using AFM and the results show that the surface roughness of PE particles is less than 1 μm (see the supplementary material [57] for details). Materials selection is based on a

density matching condition to avoid significant sedimentation of particle clusters in the no-flow direction (x_3-direction). The meniscus fluid is immiscible with the bulk fluid and wets the particles with an average contact angle $\theta = 55° \pm 4°$. A shear rheometer (DHR-2, TA Instruments) was used to measure the viscosity of the suspending and meniscus fluids ($\eta_c = 10\,\mathrm{Pa\,s}$ for silicone oil and $\eta_d = 19\,\mathrm{Pa \cdot s}$ for PIB-24). Extensional viscosity was also measured for PIB-24 using dripping-on-substrate (DoS) rheometry [37–40], showing that the liquid is Newtonian across the relevant range of strain rates in this experiment (see the supplementary material [57] for details). The selection of high viscosity fluids facilitates access to large capillary numbers Ca, as discussed below. The interfacial tension between the two fluids was measured using the droplet deformation method in extensional flow using the Stokes trap with an average value of $\sigma = 3 \pm 0.2\,\mathrm{mN/m}$ (see the supplementary material [57] for details). PE particles were imaged using environmental scanning electron microscopy (ESEM) to measure their diameter; the average particle diameter was $100 \pm 5\,\mu\mathrm{m}$ and ranged between 90 and $106\,\mu\mathrm{m}$. Meniscus-bound clusters are prepared using bulk mixing. Here, a small volume of the meniscus fluid PIB-24 (approximately $100\,\mu l$) is mixed with 1 ml of silicone oil to obtain a milky white dispersion of fine droplets. Subsequently, 100 mg of PE particles are added to the dispersion and gently mixed, allowing for collisions between particles and PIB-24 drops, thus forming capillary bridges between particles. The mixture is further diluted (at a ratio of 1:100) to obtain the final mixture used for imaging and experiments. Figure 1(c) shows a schematic of two-particle meniscus-bound cluster in planar extensional flow, trapped near the stagnation point at the center of the cross-slot in the microfluidic device. During imaging experiments, we routinely observe particle clusters with variable number of particles $N = 2, 3, 4$, and higher order clusters, however in this work, we focus only on studying particle doublets (two-particle clusters), using the Stokes trap setup.

C. Particle tracking velocimentry

Particle tracking velocimetry (PTV) is used to characterize the flow field in the microfluidic device. Fluorescent polystyrene (PS) particles ($10\,\mu\mathrm{m}$ diameter, ThermoFisher Scientific) are used for PTV experiments. The aqueous sample is first centrifuged to obtain the dense phase of PS particles, which are then resuspended in silicone oil (10 Pa s viscosity). The suspension is then sonicated (Branson 2510R-MT) for 45–50 min to obtain a well mixed particle sample for experiments. The PS particles are introduced into the device, and videos ($\approx$5 min in duration) of particles convecting in planar extensional flow are captured in the vicinity of the cross-slot as a function of strain rate $\dot{\varepsilon}$. Video files (supplementary material, Movie 1 [57]) are used as an input for image analysis where particle velocities and trajectories are determined using a custom MATLAB program, as previously described [36]. Particle velocities in the x_1 and x_2-directions are determined as a function of position, and the data are fitted to the flow field equations for planar extensional flow using the velocity gradient tensor as a fitting parameter

$$\begin{bmatrix} v_{x_1} \\ v_{x_2} \end{bmatrix} = \begin{bmatrix} a & b \\ c & d \end{bmatrix} \begin{bmatrix} x_1 \\ x_2 \end{bmatrix}. \tag{1}$$

The matrix entries a and d yield the strain rates in x_1 and x_2-directions ($\dot{\varepsilon}_{x_1}$ and $\dot{\varepsilon}_{x_2}$), respectively, and the entries b and c are found to be approximately zero. Using this approach, $\dot{\varepsilon}_{x_1}$ and $\dot{\varepsilon}_{x_2}$ are determined as a function of the input pressure in the microfluidic system [Fig. 2(a)]. Three PTV experiments are performed at each of the input pressure values, and average strain rate $\dot{\varepsilon}$ and standard deviation values are reported. Figure 2(b) shows a plot of the ratio of the strain rate in the x_1-direction to the strain rate in the x_2-direction as a function of inlet pressure, which further validates the existence of planar extensional flow (i.e., $\dot{\varepsilon}_{x_1} = -\dot{\varepsilon}_{x_2}$).
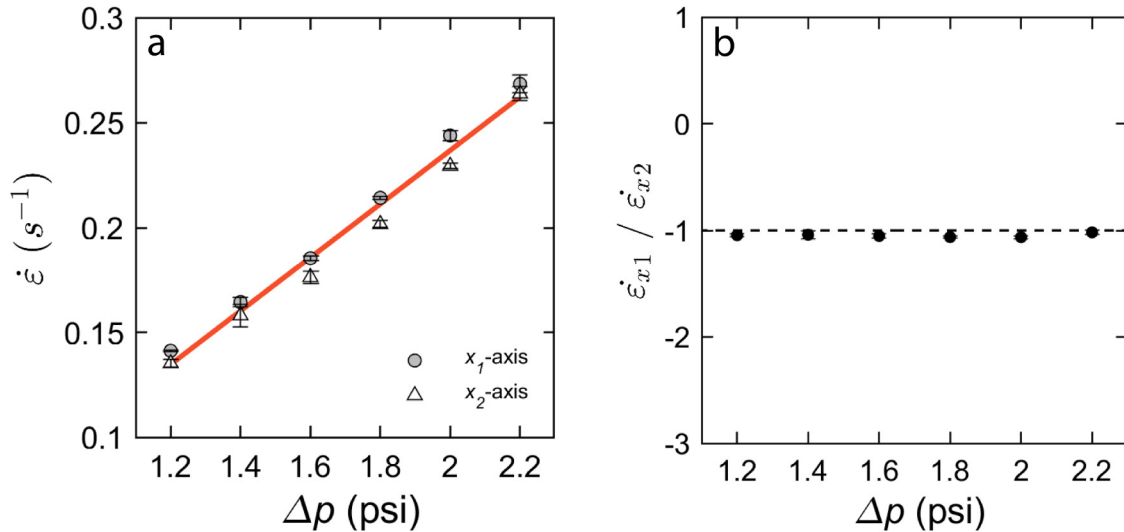
FIG. 2. Flow characterization in the cross-slot of the microfluidic device. (a) Strain rate, $\dot{\varepsilon}$, at the central plane of the microfluidic device is determined as a function of the input pressure, Δp in the channels for both x_1 and x_2 directions. Error bars show standard deviation from multiple ($\geq$3) experiments. Polystyrene (PS) particles ($10\,\mu\mathrm{m}$ in diameter) are added to silicone oil (η_c=10 Pa s) for particle tracking experiments. (b) Ratio of the strain rates in x_1 and x_2 directions is determined to be ≈ -1, thus verifying the existence of planar extensional flow in the cross-slot ($\dot{\varepsilon}_{x_1} = -\dot{\varepsilon}_{x_2}$).

III. ANALYTICAL MODEL

A. Cluster breakup

We developed an analytical model for particle cluster breakup that accounts for the forces acting on the particles as well as interparticle hydrodynamic interactions (HIs). Figure 3 shows a schematic of a two-particle liquid-bound cluster in planar extensional flow showing the relevant variables and coordinate system. The cluster breakup phenomenon in extensional flow depends on the interplay between the hydrodynamic drag forces, capillary forces, and lubrication forces between particles. All of our experiments are performed in the limit of low Reynolds numbers (particle Reynolds number, $Re_p = \rho_c R U / \eta_c \approx 10^{-7}$; and device Reynolds number, $Re_d = \rho_c H U / \eta_c \approx 10^{-6}$, where R is the particle radius, H is the channel height of the device, and U is a characteristic fluid velocity), hence inertia is neglected. In the following, we use index notation such that subscripts refer to the vector or tensorial nature of a quantity. A force balance on particle j in a two-particle cluster yields

$$F_i^{cap,j} + F_i^{vis,j} = 0 \quad j = 1 \text{ or } 2, \qquad (2)$$

where $F_i^{cap,j}$ is the capillary force on bead j and $F_i^{vis,j}$ is the net viscous force on bead j. Depending on the interparticle separation, the mathematical model for cluster breakup is described by two regimes. In the first regime, the interparticle separation D is relatively small (i.e., $D/R \lesssim 1$), such that particles experience lubrication forces, a hydrodynamic drag force from the flowing fluid and an attractive capillary force from the liquid bridge. In the second regime, the interparticle separation D is relatively large ($D/R > 1$) such that particles experience a hydrodynamic drag force from the fluid and a capillary force from the bridge until breakup. Consequently, we present two models, referred to below as the near-field and far-field models for cluster breakup in extensional flow. Motivated by prior work [18,19,41], we consider the
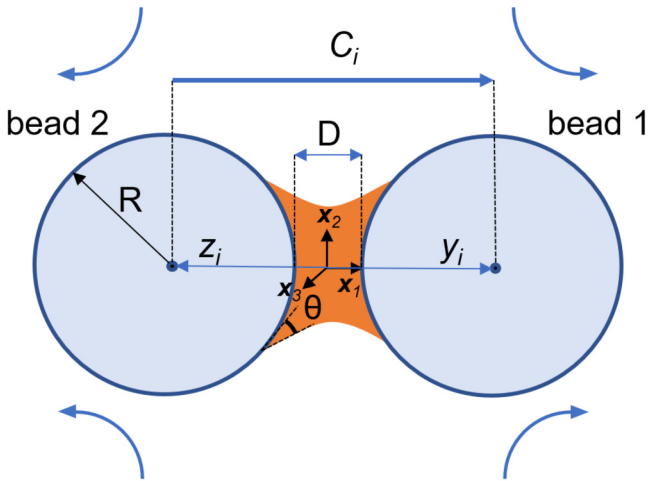

FIG. 3. Schematic of a two-particle cluster bound by a liquid bridge showing relevant parameters and the coordinate system. R is the particle radius, C_i is the vector pointing from the center of particle 2 to the center of particle 1, D is the smallest separation between the particle surfaces, y_i and z_i are the vectors pointing from the origin to the centers of particles 1 and 2, respectively, and θ is the contact angle.

lubrication approximation as valid for interparticle separations up to $D/R = 0.5$. Thus, for cluster breakup, the near-field model is considered for $D/R < 0.5$, whereas for $D/R \geq 0.5$, the far-field model is used.

1. Near-field model

The liquid bridge connecting the two particles applies an attractive capillary force that acts to pull them together [42]. An expression for the capillary force acting on a particle due to a small liquid bridge with a fixed volume was derived by Maugis [27] and reproduced by Pitois *et al.* [18]. Following the toroidal approximation, this expression assumes a small constant liquid bridge volume and a constant contact angle and is generally suitable for intermediate to small contact angle values. Using this result, the capillary force acting on bead 1 is

$$F_i^{cap,1} = -2\pi R \sigma (\cos \theta) \left[1 - \frac{1}{\sqrt{1 + \frac{2V}{\pi R D^2}}} \right] \hat{C}_i, \qquad (3)$$

where σ is the interfacial tension, θ is the contact angle, V is the liquid bridge volume, D is the smallest separation between the two particle surfaces, and $\hat{C}_i = C_i / |C_i|$ is the unit vector along the direction of separation between bead centers, as shown in the schematic in Fig. 3. From Fig. 3, also note that $y_i - z_i = C_i$.

Particles experience a net viscous force arising from the hydrodynamic drag force due to the straining motion of the suspending fluid and due to lubrication forces between particles for small interparticle separations ($D/R < 0.5$) [18,19,41]. The net viscous force on bead j is given by

$$F_i^{vis,j} = F_i^{drag,j} + F_i^{lub,j}, \qquad (4)$$

where $F_i^{drag,j}$ is the hydrodynamic drag force exerted on bead j due to flow and $F_i^{lub,j}$ is the lubrication force acting on bead j. In a transient deformation experiment, the initial state of a two-particle cluster corresponds to a small spacing between adjacent particle surfaces separated by a thin liquid film. Lubrication forces are hence expected to play a key role in determining viscous forces between particles and controlling particle dynamics. Using the Reynolds equation, Lopez *et al.* [41] calculated the pressure profile over the entire domain (meniscus and bulk suspending fluid), which was then integrated to obtain the total viscous force acting on a particle by the two fluids. Using this result, the lubrication force acting on particle 1 in the presence of a liquid bridge is

$$F_i^{lub,1} = - \left[\frac{6\pi \eta_c R^2}{\sqrt{\frac{V}{\pi R} + D^2}} + \frac{6\pi R^2}{D} \left(\sqrt{\frac{V}{\pi R} + D^2} - D \right) \right.$$
$$\left. \times \frac{\left(\eta_d \sqrt{\frac{V}{\pi R} + D^2} + D(\eta_c - \eta_d) \right)}{\frac{V}{\pi R} + D^2} \right] \frac{dD}{dt} \hat{C}_i, \qquad (5)$$

where η_d is the meniscus fluid viscosity. The derivation for Eq. (5) follows the lubrication approximation and requires that the particle surface separation must be smaller than the neck radius of the liquid bridge, which in turn must be smaller than the particle radius. These assumptions are met during the initial stages of the experiment when the interparticle separation is quite small, but they are not necessarily met for the entire duration of the experiment for larger particle separation distances [18,41]. Note that Eq. (5) includes the viscous drag force due to the center-of-mass velocity of the bead [41]. In this work, we consider cluster breakup in a planar extensional flow, which is described by a velocity field $v_i = E_{ij}x_j$, where $E_{ij} = \dot{\varepsilon}(\delta_{i1}\delta_{j1} - \delta_{i2}\delta_{j2})$ is the rate-of-strain tensor and x_j is a vector pointing from the origin. For a two-particle cluster aligned along the extensional axis, the hydrodynamic drag force on particle 1 due to the flowing fluid is approximated by Stokes' law,

$$F_i^{drag,1} \doteq 6\pi R\eta_c\dot{\varepsilon}y_i, \qquad (6)$$

where R is the particle radius, $\dot{\varepsilon}$ is the strain rate, y_i is the vector from the origin to the center-of-mass of bead 1, and η_c is the viscosity of the bulk suspending fluid. Equation (6) provides a reasonable approximation to the hydrodynamic drag force exerted on the particle in the doublet. As an aside, we validated this approximation by solving the analytical cluster breakup model while treating the numerical coefficient in Stokes' law as a fitting parameter. This analysis resulted in a good agreement between the experiments and the model and yielded a value for the numerical coefficient as ≈ 5.8, which is close to the value in Stokes drag for a sphere, thus justifying the approximation of hydrodynamic drag force using Eq. (6).

Particles also experience hydrodynamic interactions (HI) due to flow field disturbances generated by nearby particles in the cluster. Our experimental results show that the cluster breakup phenomenon in extensional flow is sensitive to small perturbations in fluid velocity, and thus we anticipate that HI plays a key role in particle cluster breakup dynamics. Here, the disturbance velocities v_i^D are calculated, and the hydrodynamic drag force is modified to account for these interactions. In the following, we consider the disturbance flow generated by particle 2 acting on particle 1 (Fig. 3). The first term in a multipole expansion of the disturbance velocity is the Stokeslet [43], which arises due to the capillary force exerted on the particles. The disturbance velocity experienced at bead 1 due to the presence of bead 2 is given by the Stokeslet

$$v_{i,(Stokeslet)}^{D,1} = G_{ij}F_j, \qquad (7)$$

where the superscript D denotes disturbance. Here, G_{ij} is the Oseen–Burgers tensor [43] and F_j is the force exerted on the fluid by the adjacent particle (taken here as bead 2) due to the capillary force. The Oseen–Burgers tensor G_{ij} is written as

$$G_{ij} = \frac{1}{8\pi\eta_c C}\left(\delta_{ij} + \frac{C_i C_j}{C^2}\right), \qquad (8)$$

where C is the center-to-center distance between particles, C_i is the vector pointing from the center of particle 2 to the center of particle 1, and δ_{ij} is the Kronecker delta. The two-particle cluster is taken to be aligned along the extensional flow axis (x_1-axis), such that the vector C_i is oriented in the positive x_1 direction and has magnitude $|C_i| = |C_1| = C$. In order to calculate the disturbance velocity experienced by bead 1 due to bead 2, F_j is taken as the force exerted on the fluid by bead 2, which is equal to the negative of the net viscous force ($-F_i^{vis,j}$) exerted on bead 2, or the positive of the capillary force on bead 2 [see Eq. (2)], such that

$$F_j^{cap,2} = F^{cap}\hat{C}_j, \qquad (9)$$

where F^{cap} is the scalar magnitude of the capillary force defined in Eq. (3) and $\hat{C}_j$ is the unit vector in the x_1 direction. The expression for the Stokeslet disturbance velocity experienced by particle 1 becomes

$$v_{i,(Stokeslet)}^{D,1} = \frac{F_{cap}}{4\pi\eta_c C}\hat{C}_i. \qquad (10)$$

The Stokeslet contribution to the disturbance velocity assumes a point force in flow. The potential dipole term in the multipole expansion would account for the finite size of a sphere translating under an imposed force. However, as a simplifying assumption, this term is not included in the disturbance velocity because the particle translational velocity is relatively small, and the potential dipole term is, therefore, negligible in magnitude compared to other dominant terms in the disturbance velocity such as the stresslet (*vide infra*).

In addition to the Stokeslet, we also account for the disturbance flow due to the straining motion of the suspending fluid by introducing the stresslet [43]. In addition, the interparticle separation is typically smaller than the particle size ($D/R < 1$) at the start of the breakup process, and we, therefore, need to account for the finite size of the particles by introducing the potential quadrupole [43]. The stresslet and potential quadrupole terms both arise due to the imposed straining flow field. Consider the case of a finite sized sphere held fixed in a general linear flow in the creeping flow regime. The total fluid velocity v_i^{total} for this flow can be written as [43]

$$v_i^{total} = v_i^\infty + v_i^D = v_i^\infty + \frac{p'x_i}{2\eta_c} + v_i^H, \qquad (11)$$

where $v_i^\infty = E_{ij}x_j$ is the undistorted fluid velocity, v_i^D is the disturbance velocity, p' is the dynamic pressure, and v_i^H is a harmonic function. The rate-of-strain tensor for planar extensional flow E_{ij} is given in matrix form as

$$E_{ij} = \begin{bmatrix} \dot{\varepsilon} & 0 & 0 \\ 0 & -\dot{\varepsilon} & 0 \\ 0 & 0 & 0 \end{bmatrix}. \qquad (12)$$

Using vector spherical harmonics, the functional forms of p' and v_i^H are

$$p' = aE_{jk}\frac{x_j x_k}{r^5} \quad \text{and} \quad v_i^H = bE_{ij}\frac{x_j}{r^3} + cT_{ijk}E_{jk}, \quad (13)$$

where a, b, and c are scalar constants and the third order tensor T_{ijk} is

$$T_{ijk} = \frac{\delta_{ij}x_k + \delta_{ik}x_j + \delta_{jk}x_i}{r^5} - \frac{5x_i x_j x_k}{r^7}. \quad (14)$$

Satisfying the continuity equation and the no-slip boundary condition on the surface of the sphere, we determine the constants a, b, and c, resulting in an expression for the total fluid velocity for the case of a sphere held fixed in planar extensional flow,

$$v_i^{total} = v_i^\infty - \frac{5R^3}{2}\frac{C_i C_j C_k}{C^5}E_{jk}$$
$$- \frac{R^5}{2}\left[\frac{\delta_{ij}C_k + \delta_{ik}C_j + \delta_{jk}C_i}{C^5} - \frac{5C_i C_j C_k}{C^7}\right]E_{jk}. \quad (15)$$

Simplifying the above equation, we obtain two additional terms contributing to the disturbance velocity on particle 1,

$$v_{i,(stresslet,\,pot.\,quad.)}^{D,1} = \left(-\frac{5\dot\varepsilon R^3}{2C^2} + \frac{3\dot\varepsilon R^5}{2C^4}\right)\hat C_i, \quad (16)$$

where the subscript "$pot.\,quad.$" stands for potential quadrupole. Using Eqs. (10) and (16), the total disturbance velocity acting on particle 1 is

$$v_i^{D,1} = v_{i,(Stokeslet)}^{D,1} + v_{i,(stresslet,\,pot.\,quad.)}^{D,1}$$
$$= \left(\frac{F_{cap}}{4\pi\eta_c C} - \frac{5\dot\varepsilon R^3}{2C^2} + \frac{3\dot\varepsilon R^5}{2C^4}\right)\hat C_i. \quad (17)$$

Similarly, the disturbance velocity acting on particle 2 can be determined using an analogous set of arguments as above.

The force balance on particle 1 becomes

$$6\pi R\eta_c(\dot\varepsilon y_i + v_i^{D,1}) - 2\pi R\sigma\cos\theta\left[1 - \frac{1}{\sqrt{1 + \frac{2V}{\pi RD^2}}}\right]\hat C_i$$
$$- \left[\frac{6\pi\eta_c R^2}{\sqrt{\frac{V}{\pi R} + D^2}} + \frac{6\pi R^2}{D}\left(\sqrt{\frac{V}{\pi R} + D^2} - D\right)\right.$$
$$\left.\times \frac{\left(\eta_d\sqrt{\frac{V}{\pi R} + D^2} + D(\eta_c - \eta_d)\right)}{\frac{V}{\pi R} + D^2}\right]\frac{dD}{dt}\hat C_i = 0. \quad (18)$$

Similarly, a force balance on particle 2 gives

$$6\pi R\eta_c(\dot\varepsilon z_i + v_i^{D,2}) + 2\pi R\sigma\cos\theta\left[1 - \frac{1}{\sqrt{1 + \frac{2V}{\pi RD^2}}}\right]\hat C_i$$
$$+ \left[\frac{6\pi\eta_c R^2}{\sqrt{\frac{V}{\pi R} + D^2}} + \frac{6\pi R^2}{D}\left(\sqrt{\frac{V}{\pi R} + D^2} - D\right)\right.$$
$$\left.\times \frac{\left(\eta_d\sqrt{\frac{V}{\pi R} + D^2} + D(\eta_c - \eta_d)\right)}{\frac{V}{\pi R} + D^2}\right]\frac{dD}{dt}\hat C_i = 0. \quad (19)$$

Equation (18) is subtracted from (19), allowing the force balance to be expressed in terms of the vector connecting the bead centers C_i. We assume that the two-particle cluster is aligned along the extensional flow axis (x_1-axis), which simplifies the force balance to a scalar equation along the x_1-axis. This equation is simplified and nondimensionalized to obtain a first-order differential equation for the dimensionless interparticle separation between bead surfaces $D^*(t^*)$,

$$\frac{dD^*}{dt^*} = \frac{Ca\left(3C^* - \frac{15}{C^{*2}} + \frac{9}{C^{*4}}\right)}{\frac{6}{K^*} + \frac{6(K^* - D^*)(\eta_r K^* + D^*(1 - \eta_r))}{D^* K^{*2}}}$$
$$+ \frac{\cos\theta\left(\frac{3}{C^*} - 2\right)\left[1 - \frac{1}{\sqrt{1 + \frac{2V^*}{\pi D^{*2}}}}\right]}{\frac{6}{K^*} + \frac{6(K^* - D^*)(\eta_r K^* + D^*(1 - \eta_r))}{D^* K^{*2}}}, \quad (20)$$

where the superscript * denotes a dimensionless quantity. Equation (20) is nondimensionalized using the particle radius R and the characteristic time scale $t_c = R\eta_c/\sigma$. The capillary number $Ca = \dot\varepsilon R\eta_c/\sigma$ is the ratio of the viscous to interfacial tension forces. The relative viscosity is $\eta_r = \eta_d/\eta_c = 1.9$ for our experimental conditions. The quantity K^* is defined as $K^* = \sqrt{\frac{V^*}{\pi} + D^{*2}}$, and the dimensionless center-to-center distance is $C^* = D^* + 2$. Here, $C = D + 2R$ and $D^* = D/R$. Equation (20) is considered for interparticle separations $D/R < 0.5$.

2. Far-field model

The far-field model is considered for relatively large interparticle separations ($D/R \geq 0.5$). Here, lubrication forces are not included in the viscous force term $F_i^{vis,j}$. However, the net hydrodynamic drag force is modified to include the center-of-mass bead velocity

$$F_i^{drag,1} = 6\pi R\eta_c(\dot\varepsilon y_i - \dot y_i), \quad (21)$$

such that the net viscous force $F_i^{vis,j}$ is now given by $F_i^{drag,j}$ in Eq. (2). The capillary force and the disturbance velocity terms remain the same as the near-field model, and the force

balance on particle 1 is written as

$$6\pi R \eta_c(\dot{\varepsilon}y_i + v_i^{D,1} - \dot{y}_i) - 2\pi R \sigma \cos\theta \left[1 - \frac{1}{\sqrt{1 + \frac{2V}{\pi R D^2}}}\right]\hat{C}_i = 0.$$

(22)

Similarly, for particle 2,

$$6\pi R \eta_c(\dot{\varepsilon}z_i + v_i^{D,2} - \dot{z}_i) + 2\pi R \sigma \cos\theta \left[1 - \frac{1}{\sqrt{1 + \frac{2V}{\pi R D^2}}}\right]\hat{C}_i = 0.$$

(23)

Subtracting Eq. (22) from (23), simplifying and nondimensionalizing, we obtain a dimensionless first-order differential equation for the interparticle separation $D^*(t^*)$,

$$\frac{dD^*}{dt^*} = Ca\left(C^* - \frac{5}{C^{*2}} + \frac{3}{C^{*4}}\right)$$
$$+ \cos\theta\left(\frac{1}{C^*} - \frac{2}{3}\right)\left[1 - \frac{1}{\sqrt{1 + \frac{2V^*}{\pi D^{*2}}}}\right].$$

(24)

Thus, from Eqs. (20) and (24), we obtain

$$\frac{dD^*}{dt^*} = \begin{cases} \dfrac{Ca\left(3C^* - \dfrac{15}{C^{*2}} + \dfrac{9}{C^{*4}}\right)}{\dfrac{6}{K^*} + \dfrac{6(K^* - D^*)(\eta_r K^* + D^*(1 - \eta_r))}{D^* K^{*2}}} + \dfrac{\cos\theta\left(\dfrac{3}{C^*} - 2\right)\left[1 - \dfrac{1}{\sqrt{1 + \frac{2V^*}{\pi D^{*2}}}}\right]}{\dfrac{6}{K^*} + \dfrac{6(K^* - D^*)(\eta_r K^* + D^*(1 - \eta_r))}{D^* K^{*2}}}, & \dfrac{D}{R} < 0.5, \\[4mm] Ca\left(C^* - \dfrac{5}{C^{*2}} + \dfrac{3}{C^{*4}}\right) + \cos\theta\left(\dfrac{1}{C^*} - \dfrac{2}{3}\right)\left[1 - \dfrac{1}{\sqrt{1 + \frac{2V^*}{\pi D^{*2}}}}\right], & \dfrac{D}{R} \geq 0.5. \end{cases}$$

(25)

Note that $C^* = D^* + 2$. Additionally, from Eq. (24), in the limit of large D^*, we recover the limit of freely suspended individual particles (such that particles follow fluid streamlines) where particles are assumed to flow freely in planar extensional flow in the absence of any additional forces, i.e., $dC^*/dt^* = C^*$.

3. Predicting a critical capillary number Ca_{crit} for cluster breakup

The analytical model developed above for a two-particle liquid-bound cluster breakup can be used to predict the critical capillary number Ca_{crit} for cluster breakup in planar extensional flow. The interplay between various forces during the initial stages of deformation plays a major role in cluster separation. We, therefore, consider the near-field model [Eq. (20)] as given above for this discussion. Equation (20) can be written in a compact form as follows:

$$\frac{dD^*}{dt^*} = \frac{K^*}{6}\left[Ca \cdot f(C^*) + \cos\theta\left(\frac{3}{C^*} - 2\right)g\left(\frac{V^*}{D^{*2}}\right)\right]\frac{1}{h}, \quad (26)$$

where f, g, and h are functions of system parameters. In particular, f is a function of C^* defined as

$$f(C^*) = 3C^* - \frac{15}{C^{*2}} + \frac{9}{C^{*4}}, \quad (27)$$

and g is a function defined as

$$g\left(\frac{V^*}{D^{*2}}\right) = \left[1 - \frac{1}{\sqrt{1 + \frac{2V^*}{\pi D^{*2}}}}\right]. \quad (28)$$

Finally, h is defined as

$$h = 1 + \left(1 - \frac{D^*}{K^*}\right)\left(\eta_r\frac{K^*}{D^*} + (1 - \eta_r)\right). \quad (29)$$

Given an initial condition of near contact between particles, cluster separation requires $dD^*/dt^* > 0$. Because $K^* > D^*$ and $h > 0$, the condition for breakup, therefore, requires

$$Ca \cdot f(C^*) + \cos\theta\left(\frac{3}{C^*} - 2\right)g\left(\frac{V^*}{D^{*2}}\right) > 0. \quad (30)$$

At time $t = 0$, the initial smallest separation between particle surfaces D_0 is defined to be $D_0 = 3\,\mu$m (see Sec. IV), which yields $D^* = 0.06$. Hence, $C^* = 2.06$ and $f(2.06) = 3.15$. Furthermore, liquid bridge volumes for our experiments typically lie in the range of 1500–2000 μm^3, thus $V^* = V/R^3$ is of the order 0.01. Assuming a value of $V^* = 0.01$, $g\left(\frac{V^*}{D^{*2}}\right) \approx 0.4$, which simplifies Eq. (30) to

$$Ca_{crit} \approx \frac{\cos\theta}{14.3}. \quad (31)$$

Substituting the average value of $\theta = 55°$ for our experiments (see Sec. II), we obtain a critical capillary number value of $Ca_{crit} = 0.04$, which is in reasonable agreement with the Ca values observed in our experiments (Sec. IV). Thus, Eq. (30) provides a simple prediction of an approximate Ca_{crit} for a capillary suspension breakup in extensional flow.

B. Cluster relaxation

In this section, we develop a model for cluster relaxation dynamics under zero-flow conditions. In our experiments, a two-particle cluster is trapped near the stagnation point, subjected to extensional flow for a finite time, and the flow is then switched off before cluster breakup occurs. The cluster is then allowed to relax under zero-flow conditions, where the liquid bridge draws the particles together due to capillary forces. Similar to the cluster breakup model, we again develop a near-field and far-field model for the problem. At the beginning of the experiment, the two-particle cluster is significantly deformed and the particles are far apart; hence, lubrication forces are not included in the far-field model. However, after the cluster relaxes due to the attractive capillary force, the particles eventually experience a repulsive lubrication force upon close approach due to the thin liquid film in the gap between particles.

1. Far-field model

In the far-field model, lubrication forces are not included in the viscous force $F_i^{vis,j}$ due to the relatively large interparticle separation. In addition, cluster relaxation occurs under zero-flow conditions. Therefore, the net viscous force arises due to the hydrodynamic drag force on a particle due to its center-of-mass velocity and the disturbance velocity due to hydrodynamic interactions. The drag force on particle 1 is given by

$$F_i^{drag,1} = 6\pi R\eta_c(v_i^{D,1} - \dot{y}_i). \quad (32)$$

The capillary force on particle 1 due to the liquid bridge [Eq. (3)] is the same as in the case of cluster breakup. In addition, the disturbance velocity only includes the Stokeslet contribution because of the zero-flow conditions

$$v_i^{D,1} = \frac{F_{cap}}{4\pi\eta_c C}\hat{C}_i. \quad (33)$$

For cluster relaxation, we account for excluded volume interactions between the spheres. Here, we introduce the Weeks–Chandler–Anderson (WCA) potential, which is the repulsive part of the Lennard-Jones potential. We found that the repulsive potential is needed to capture the physics of near-sphere interaction more accurately. In addition, owing to the polydispersity in the particle size in experiments, perfect quantitative agreement is not expected between experiments and the analytical model. The WCA potential can be defined in terms of the Lennard-Jones potential as follows:

$$V_{WCA}(r) = \begin{cases} V_{LJ}(r) + \varepsilon_{LJ}, & \text{if } r < 2^{1/6}(C_0), \\ 0, & \text{if } r \geq 2^{1/6}(C_0), \end{cases} \quad (34)$$

where the Lennard-Jones potential is given by

$$V_{LJ} = 4\varepsilon_{LJ}\left[\left(\frac{C_0}{C}\right)^{12} - \left(\frac{C_0}{C}\right)^6\right]. \quad (35)$$

Here, ε_{LJ} is the depth of the potential well and is chosen as the characteristic surface energy (σR^2) for our system, C_0 is the distance at which the potential energy is zero, and C is the distance between the particle centers. Differentiating Eq. (34), we obtain the repulsive force from the WCA potential on particle 1,

$$F_i^{WCA,1} = \begin{cases} \frac{4\varepsilon_{LJ}}{C}\left[12\left(\frac{C_0}{C}\right)^{12} - 6\left(\frac{C_0}{C}\right)^6\right]\hat{C}_i, & \text{if } C < 2^{1/6}C_0, \\ 0, & \text{if } C \geq 2^{1/6}C_0. \end{cases} \quad (36)$$

The force balance on particle 1 can now be written as

$$6\pi R\eta_c(v_i^{D,1} - \dot{y}_i)$$
$$- 2\pi R\sigma\cos\theta\left[1 - \frac{1}{\sqrt{1 + \frac{2V}{\pi RD^2}}}\right]\hat{C}_i + F_i^{WCA,1} = 0. \quad (37)$$

Similarly, for particle 2,

$$6\pi R\eta_c(v_i^{D,2} - \dot{z}_i)$$
$$+ 2\pi R\sigma\cos\theta\left[1 - \frac{1}{\sqrt{1 + \frac{2V}{\pi RD^2}}}\right]\hat{C}_i + F_i^{WCA,2} = 0. \quad (38)$$

Subtracting Eq. (37) from (38), simplifying and nondimensionalizing, we obtain a dimensionless first-order differential equation for the interparticle spacing D^* describing cluster relaxation,

$$\frac{dD^*}{dt^*} = \cos\theta\left(\frac{1}{C^*} - \frac{2}{3}\right)\left[1 - \frac{1}{\sqrt{1 + \frac{2V^*}{\pi D^{*2}}}}\right] + \frac{F_{WCA}^*}{3}, \quad (39)$$

where F_{WCA}^* is the scalar dimensionless force from the WCA potential given as

$$F_{WCA}^* = \begin{cases} \frac{\varepsilon_c}{C^*}\left[12\left(\frac{C_0^*}{C^*}\right)^{12} - 6\left(\frac{C_0^*}{C^*}\right)^6\right], & \text{if } C^* < 2^{1/6}(C_0^*), \\ 0, & \text{if } C^* \geq 2^{1/6}(C_0^*), \end{cases} \quad (40)$$

where ε_c is the dimensionless dispersion energy defined as $\varepsilon_c = 4\varepsilon_{LJ}/\pi\sigma R^2$ and is taken as a fitting parameter in the model.

As the cluster begins to relax and the particles approach each other, lubrication forces will begin to play a role in the process. In our experiments, we observe a marked decrease in the rate of cluster relaxation at a finite interparticle separation, which occurs when lubrication forces begin to play a

role in the relaxation process (see Fig. 9). Based on our experimental data, we define the transition point from the far-field to the near-field model when $\approx 75\%$ of the relaxation has occurred. Therefore, the far-field model is assumed to transition to the near-field model at a dimensionless interparticle spacing of $D/R = 0.2$ during cluster relaxation.

2. Near-field model

In the near-field case, the particles experience a repulsive lubrication force due to the thin liquid film. As discussed above, the lubrication force given by Eq. (5) accounts for the particle approach velocity (and hence viscous drag due to particle center-of-mass motion). Therefore, the hydrodynamic drag force only accounts for the disturbance velocity at particle 1,

$$F_i^{drag,1} = 6\pi R\eta_c v_i^{D,1}. \tag{41}$$

Combining the expressions for the capillary force and excluded volume forces from Eqs. (3) and (36) respectively, the force balance on particle 1 is given as

$$6\pi R\eta_c v_i^{D,1} - 2\pi R\sigma \cos\theta \left[1 - \frac{1}{\sqrt{1 + \frac{2V}{\pi RD^2}}}\right]\hat{C}_i + F_i^{WCA,1}$$

$$- \left[\frac{6\pi\eta_c R^2}{\sqrt{\frac{V}{\pi R} + D^2}} + \frac{6\pi R^2}{D}\left(\sqrt{\frac{V}{\pi R} + D^2} - D\right)\right.$$

$$\left. \times \frac{\left(\eta_d\sqrt{\frac{V}{\pi R} + D^2} + D(\eta_c - \eta_d)\right)}{\frac{V}{\pi R} + D^2}\right]\frac{dD}{dt}\hat{C}_i = 0. \tag{42}$$

Similarly, a force balance on particle 2 yields

$$6\pi R\eta_c v_i^{D,2} + 2\pi R\sigma \cos\theta \left[1 - \frac{1}{\sqrt{1 + \frac{2V}{\pi RD^2}}}\right]\hat{C}_i + F_i^{WCA,2}$$

$$+ \left[\frac{6\pi\eta_c R^2}{\sqrt{\frac{V}{\pi R} + D^2}} + \frac{6\pi R^2}{D}\left(\sqrt{\frac{V}{\pi R} + D^2} - D\right)\right.$$

$$\left. \times \frac{\left(\eta_d\sqrt{\frac{V}{\pi R} + D^2} + D(\eta_c - \eta_d)\right)}{\frac{V}{\pi R} + D^2}\right]\frac{dD}{dt}\hat{C}_i = 0. \tag{43}$$

Following a similar procedure as explained above, we obtain a dimensionless first-order differential equation for interparticle separation D^* for the near-field case of cluster relaxation,

$$\frac{dD^*}{dt^*} = \frac{\cos\theta\left(\frac{3}{C^*} - 2\right)\left[1 - \frac{1}{\sqrt{1 + \frac{2V^*}{\pi D^{*2}}}}\right] + F_{WCA}^*}{\frac{6}{K^*} + \frac{6(K^* - D^*)(\eta_r K^* + D^*(1 - \eta_r))}{D^* K^{*2}}}. \tag{44}$$

Taken together, Eqs. (39) and (44) provide a model for cluster relaxation in terms of a dimensionless interparticle separation $D^*(t^*)$,

$$\frac{dD^*}{dt^*} = \begin{cases} \cos\theta\left(\frac{1}{C^*} - \frac{2}{3}\right)\left[1 - \frac{1}{\sqrt{1 + \frac{2V^*}{\pi D^{*2}}}}\right] + \frac{F_{WCA}^*}{3}, & \frac{D}{R} > 0.2, \\[2em] \dfrac{\cos\theta\left(\frac{3}{C^*} - 2\right)\left[1 - \frac{1}{\sqrt{1 + \frac{2V^*}{\pi D^{*2}}}}\right] + F_{WCA}^*}{\frac{6}{K^*} + \frac{6(K^* - D^*)(\eta_r K^* + D^*(1 - \eta_r))}{D^* K^{*2}}}, & \frac{D}{R} \leq 0.2. \end{cases} \tag{45}$$

Note that $C^* = D^* + 2$. In the limit of small D^*, the near-field equations for both breakup and relaxation predict exponential separation or approach of particles, respectively.

IV. RESULTS

A. Cluster breakup

We began by experimentally observing cluster breakup for two-particle clusters using a Stokes trap. In this experiment, we measured the cluster breakup time as a function of strain rate $\dot{\varepsilon}$ or capillary number Ca, defined as

$$Ca = \frac{\dot{\varepsilon}R\eta_c}{\sigma}. \tag{46}$$

Two-particle clusters are introduced into the cross-slot device. A target cluster is trapped and positioned to be located near the center of the cross-slot, and the flow is switched off. Two-particle clusters near the center plane of the flow device (in the x_3-direction) were considered for this work. The experiment begins by turning on the planar extensional flow while confining the cluster near the stagnation point using the Stokes trap. For consistency, time $t = 0$ in all experiments is defined at the time at which interparticle separation is $D = 3\,\mu$m using image analysis (see below). After the extensional flow is turned on, the two-particle cluster reorients and aligns along the direction of the principal axis of extension. The cluster is then subjected to extensional flow until the meniscus stretches and ultimately ruptures, leading to cluster breakup (supplementary material, Movie 2 [57]). The transient cluster breakup process is shown in Fig. 4(a), where the center-to-center distance between particles in a two-particle cluster is shown for $Ca = 0.035$. Figures 4(b), 4(c), and 4(d) show snapshots of the cluster at different times during the breakup process. Figure 4(b) shows the cluster at $t = 0$ s, when the cluster has already reoriented. Figure 4(c) shows the cluster at $t = 36$ s, when the meniscus has stretched into a thin thread immediately prior to rupture. Figure 4(d) shows an image of the system at time $t = 39$ s, which occurs after the cluster has broken up and the two particles are separated in flow. After the meniscus ruptures and the cluster has broken up, the particles rapidly separate as a function of time in flow.

Images of cluster breakup events from experiments are analyzed using a MATLAB program. The image is first
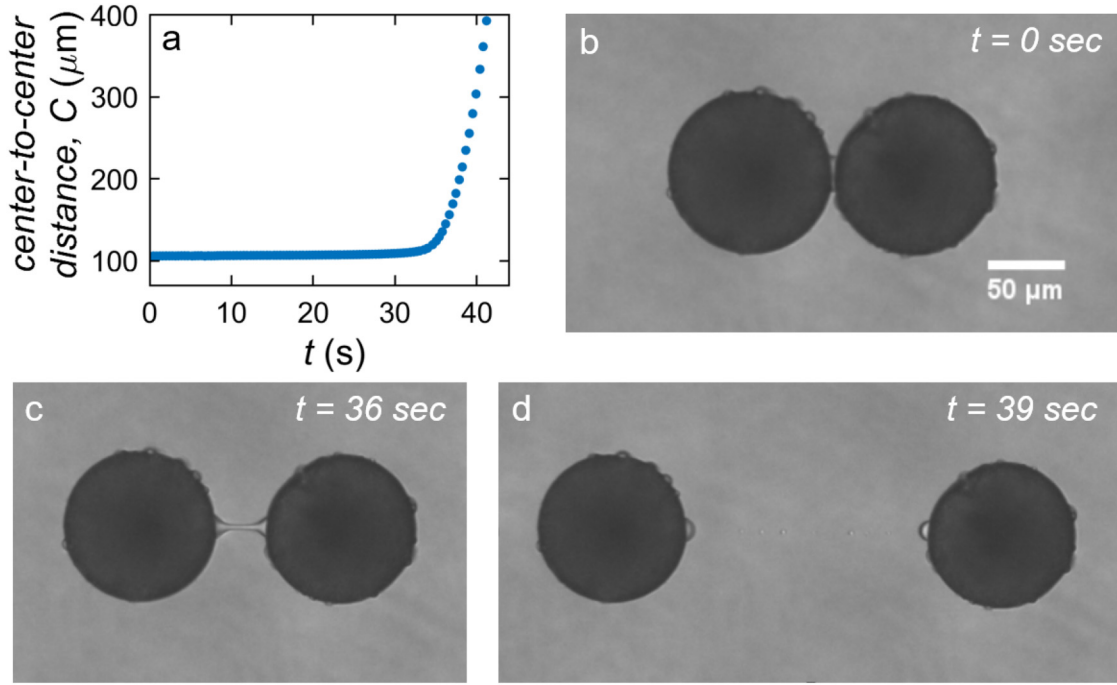
FIG. 4. Experiments on two-particle cluster breakup in extensional flow. (a) Center-to-center distance C plotted as a function of time for a two-particle cluster breakup for $Ca = 0.035$. (b) Snapshot of the cluster at $t = 0$ s. For consistency, time $t = 0$ in all experiments is defined as the time at which interparticle separation is $D = 3\,\mu$m. (c) Snapshot of the cluster at $t = 36$ s. Here, the cluster has started to separate and the meniscus is stretched into a thin thread. (d) Snapshot of the cluster at $t = 39$ s, which occurs after the cluster is completely broken up.

binarized and impurities surrounding the cluster are removed. To identify and track individual particles in the two-particle cluster, a watershed segmentation algorithm is used [44,45]. The centroid positions of each particle are then determined, which enables calculation of the center-to-center distance C. Breakup experiments are performed until the meniscus is completely broken, which occurs when C is approximately four times larger than its initial value, i.e., roughly four times the particle diameter. Using this method, we quantify the interparticle separation as a function of time during a cluster breakup experiment, as shown in Fig. 4(a).

Results from cluster breakup experiments are compared to the analytical model developed in Sec. III. The first-order differential equation for cluster breakup [given by Eq. (25)] is solved numerically using the fourth-order Runge–Kutta method (RK4). After solving Eq. (25) for the dimensionless interparticle separation D^*, the quantities are converted back to their dimensional forms using the relations $t^* = t/t_c$, where the characteristic time scale is $t_c = R\eta_c/\sigma$, and $C = (D^* + 2)R$, enabling direct comparison with experiments. Due to limitations in spatial resolution in optical imaging experiments, the initial value of D at time $t = 0$ may vary slightly ($D_0 = 3 \pm 1.6\,\mu$m) between different experiments. Therefore, a nonlinear least squares analysis is used to fit the experimental data to the numerical solution by treating D_0 as a fitting parameter. We note that for the cluster breakup model, D_0 is the *only* fitting parameter used when comparing to experimental data.

Figure 5 provides a comparison between cluster breakup experiments and the analytical model, generally showing good agreement for two different flow strengths ($Ca = 0.031$ and $Ca = 0.041$). Using the nonlinear least squares analysis,

the initial values D_0 for the data shown in Figs. 5(a) and 5(b) are $D_0 = 4.6$ *and* $3.0\,\mu$m, respectively. The contact angle θ is measured using image analysis software (IMAGEJ), and the meniscus volume V is determined using image analysis (see the supplementary material [57] for details). Our results show that the meniscus volume V typically lies in the range 1500–$2000\,\mu$m^3. In addition, the model shows that lubrication and capillary forces generally dominate for small particle separations $(D/R < 0.5)$. As D gradually increases, F^*_{drag}/F^*_{cap} becomes greater than 1 and starts increasing rapidly for $D/R > 0.5$. For larger particle separations, the hydrodynamic drag force dominates and the meniscus rapidly stretches and thins, eventually resulting in cluster breakup. Overall, the analytical model accurately captures the breakup dynamics of two-particle meniscus-bound clusters in extensional flow.

We further examined the role of interparticle hydrodynamic interactions (HI) on the cluster breakup process. Figure 6(a) shows a comparison between analytical models for cluster breakup with HI (i.e., Stokeslet, stresslet, and potential dipole interactions between beads) and without HI. The model incorporating HI yields good agreement with experiments. However, the model without HI does not predict cluster breakup, and the particles never separate under identical flow conditions. This comparison reveals the sensitivity of the breakup process to small perturbations in the flow around the particles and emphasizes the importance of interparticle HI. We note that the analytical model presented here only considers first-order interactions between beads and does not consider higher order corrections via the method of reflections, i.e., second-order and higher reflections are not considered here [46]. Nevertheless, higher order
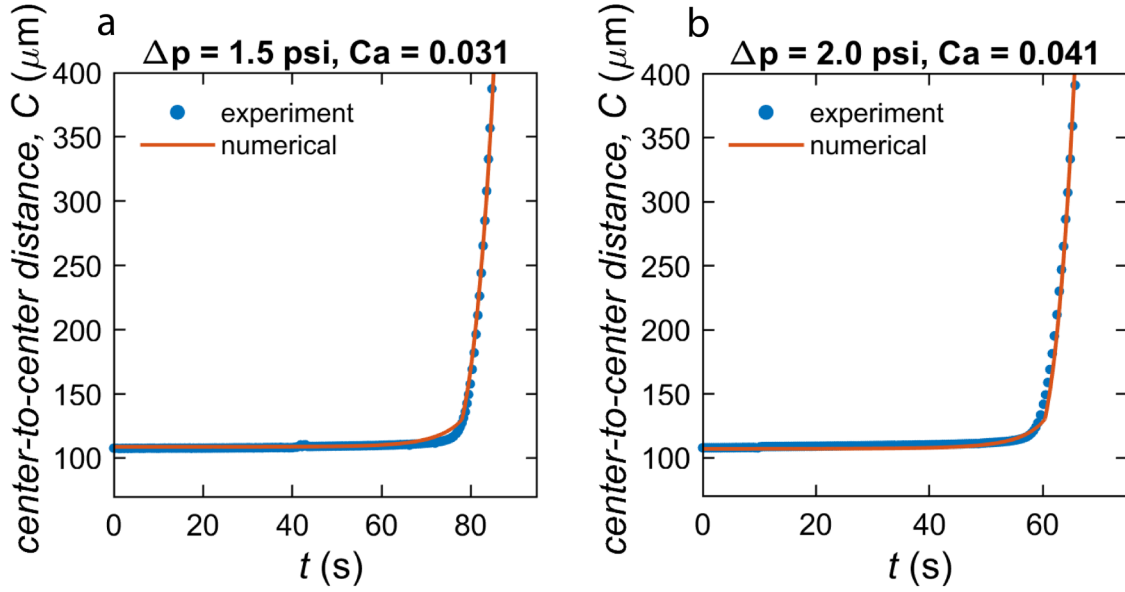
FIG. 5. Center-to-center distance C between particles plotted as a function of time for cluster breakup for two different Ca, (a) $Ca = 0.031$ and (b) $Ca = 0.041$. The blue scatter points represent the experimental data which is obtained through image analysis at each frame, and the solid orange line corresponds to the analytical model for cluster breakup where a first order differential equation is solved numerically using RK4, yielding good agreement with the experiments.

corrections are not expected to contribute to significant differences in the general qualitative behavior or outcomes observed here. The next higher order term ($\mathcal{O}(1/C^5)$) in the multipole expansion is $\approx$20 times smaller than the Stokeslet interaction. We also probed the effect of changing the transition point D_{switch}/R when the analytical model switches from the near-field to the far-field case (Sec. III). Figure 6(b) shows the comparison for various D_{switch}/R; our results show that changing the transition point value of $D_{switch}/R = 0.5$ does not qualitatively affect the results. In brief, immediately prior to cluster breakup, the meniscus begins to rapidly

stretch and D changes rapidly. Therefore, the transition point D_{switch}/R plays a relatively minor role on the numerical results, as shown in Fig. 6(b).

We next investigated the dependence of cluster breakup time on capillary number Ca and liquid bridge volume V. Based on the cluster breakup analytical model in Sec. III, we observe that given a Ca and V value, Eq. (25) can be solved to compute the corresponding cluster breakup time. Figure 7(a) shows this variation where the dimensionless cluster breakup time $t^*_{rupture}$ is plotted as a function of Ca for various liquid bridge volumes as indicated in the legend.
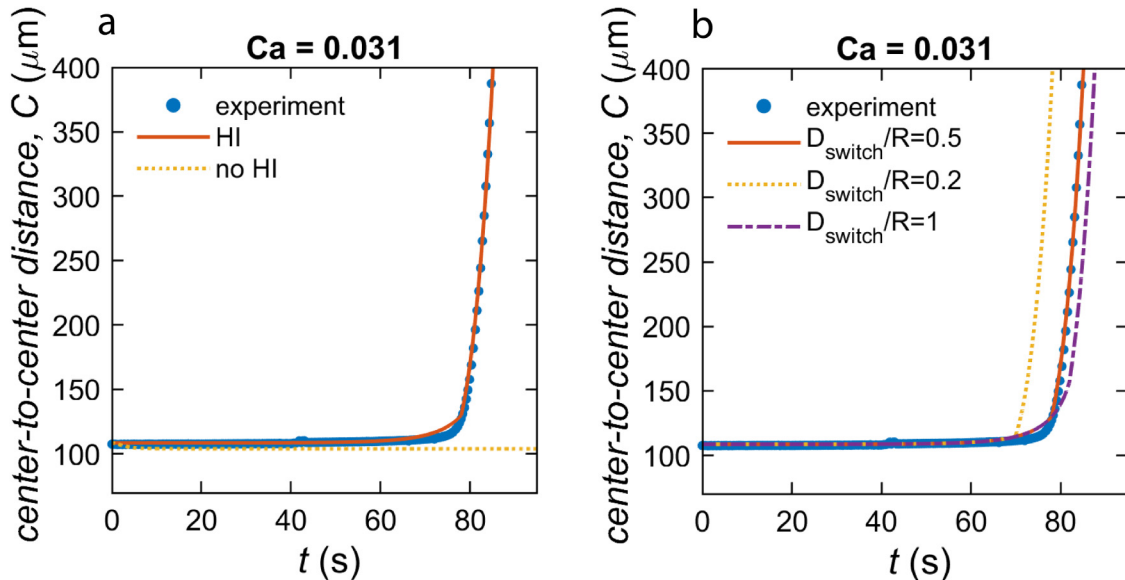

FIG. 6. Role of interparticle hydrodynamic interactions (HI) and transition between near-field and far-field model on cluster breakup dynamics. (a) Cluster breakup analytical models with and without including HI are shown. For the case with no HI, the model does not predict cluster breakup, and the particles do not separate in flow. (b) Effect of varying the transition point D_{switch}/R at which the model switches from the near-field to the far-field case.
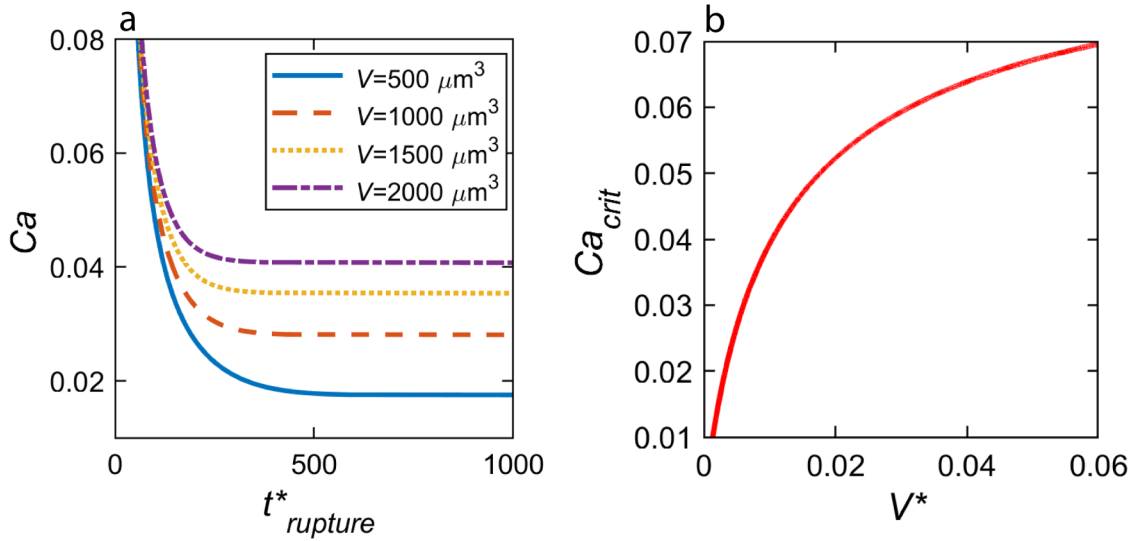
FIG. 7. The dependence of cluster breakup time on Ca and V and the prediction of a critical capillary number Ca_{crit} for two-particle clusters in extensional flow. (a) Dimensionless breakup time $t^*_{rupture}$ is plotted as a function of Ca for selected values of V using the results from the analytical model. (b) Ca_{crit} is plotted as a function of the dimensionless liquid bridge volume V^*.

Similar to the experiments, cluster breakup is considered to occur when C is approximately a factor of four larger than the initial value. It can be seen from the figure that below a certain value of Ca, $t^*_{rupture}$ increases rapidly and the curve flattens out. This turning point in the plot can be interpreted as the critical capillary number Ca_{crit} for a given liquid bridge volume, below which rupture does not occur. Furthermore, using the expression for predicting Ca_{crit} as derived in Sec. III [Eq. (30)], we plot Ca_{crit} as a function of dimensionless liquid bridge volume V^*, as shown in Fig. 7(b). Experimentally, we observe that for flow strengths below the Ca_{crit} line in Fig. 7(b), clusters with liquid bridge volumes within the range indicated generally do not separate. For these calculations, the average contact angle is $\theta = 55°$ and the $D^* = 0.06$.

B. Cluster relaxation

We further studied cluster relaxation under zero-flow conditions. The first part of the experimental procedure is similar to the cluster breakup experiment. Here, two-particle clusters are trapped near the stagnation point in the cross-slot device and subjected to planar extensional flow. However, in the cluster relaxation experiment, as the meniscus begins to stretch, the flow is stopped immediately prior to separation, and the cluster is allowed to relax under zero-flow conditions (supplementary material, Movie 3 [57]).

Figures 8(a) and 8(b) show two different stages of a two-particle cluster during relaxation. Figure 8(a) shows a snapshot of the cluster at $t = 47$ s when the flow is stopped prior to cluster breakup. The snapshot in Fig. 8(b) shows the
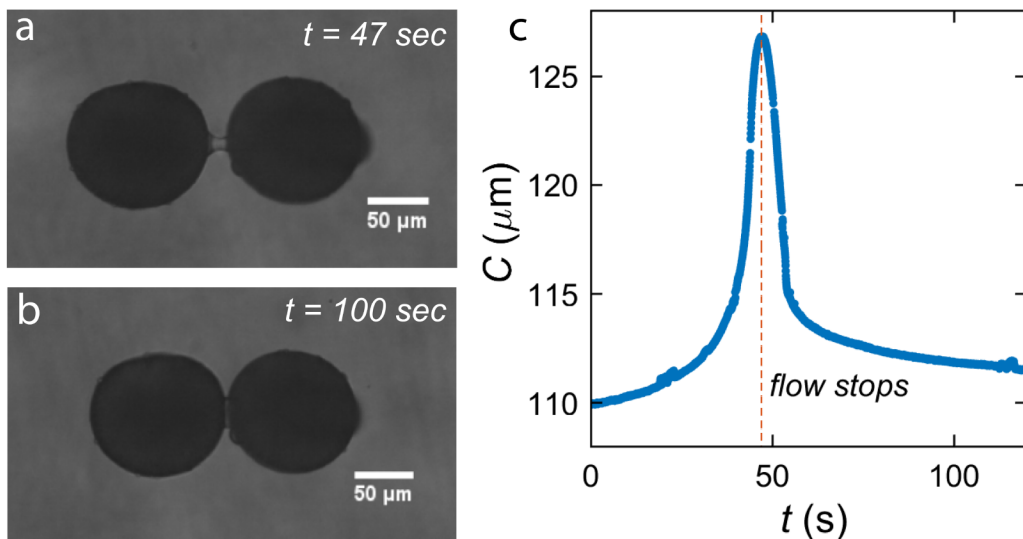
FIG. 8. Two-particle cluster relaxation under zero-flow conditions. (a) Snapshot of a two-particle cluster at $t = 47$ s, where the meniscus is stretched to the point immediately prior to rupture and the flow is turned off. Following cessation of flow, the cluster begins to relax, and the particles come closer to each other. (b) Snapshot of the cluster at a later time ($t = 100$ s), when the cluster has sufficiently relaxed and particle separation is close to the initial separation. (c) Center-to-center distance, C plotted as a function of time for cluster stretching and relaxing. The red dashed line marks the instance when the flow is turned off and the cluster begins to relax ($t = 47$ s).

two-particle cluster at a later time following cessation of flow, after which the meniscus has sufficiently relaxed and the interparticle distance is close to the initial separation. Figure 8(c) shows the interparticle separation C as a function of time for both the deformation and relaxation phase of the two-particle cluster. The red dashed line marks the instant in time when the flow is turned off, which defines the start time of the relaxation experiment. Equation (45) is solved numerically to determine D^* as a function of time using the RK4 method, and the results are compared with three different relaxation experiments. As described in Sec. III, the dimensionless dispersion energy ε_c [Eq. (40)] is used as a fitting parameter, and a nonlinear least squares analysis is used to fit the experimental data to the analytical solution. Here, $\varepsilon_c = 0.25$, which validates our choice of ε_{LJ} to be of the order of the characteristic surface energy σR^2. Generally, the dispersion energy for soft sphere potential is chosen to be of the order of $k_B T$ in the literature [47–49]. However, the model required a slightly stronger magnitude repulsion to prevent particles from passing into each other. Because the characteristic surface energy for the system is $\sigma R^2 \approx 10^9$ $k_B T$, ε_{LJ} was taken to be of a similar order as σR^2. The distance C_0 at which the potential energy V_{LJ} is zero [Eqs. (35) and (36)] is $C_0 = 105 \, \mu m$ for the model. The dimensionless quantities are converted back to their dimensional forms for direct comparison with experiments (Fig. 9). Our results generally show good agreement between experiments and the analytical model for particle cluster relaxation following cessation of extensional flow. Transient relaxation data are plotted until the cluster has relaxed to a final C value within 2% of the initial C value at time $t = 0$ in Fig. 8(c).

Cluster relaxation experiments clearly show two different regimes of relaxation dynamics. In particular, cluster relaxation begins with a rapid retraction of the liquid bridge that
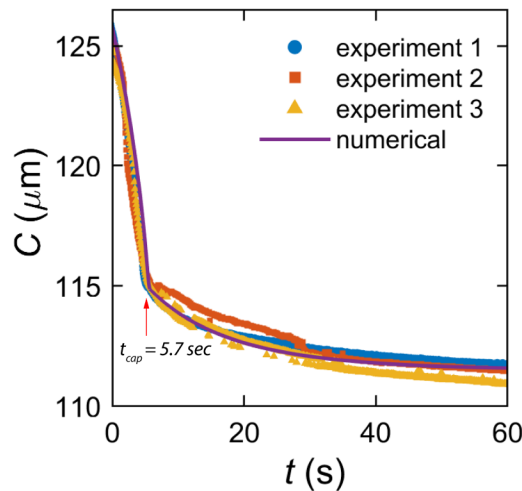

FIG. 9. Center-to-center distance C plotted as a function of time for cluster relaxation under zero-flow conditions. Experimental data is plotted for three different cluster relaxation experiments and is compared with the analytical model obtained by numerically solving the first-order differential equation for cluster relaxation (Sec. III). Our results show two modes of relaxation: an initial fast mode, dominated by the capillary force, and a second, slower mode dominated by lubrication forces. In solving the analytical model, the initial value for D is chosen to be $D_0 = 22 \, \mu m$ to match experiments. The contact angle is $\theta = 50°$ and the meniscus volume $V \approx 2000 \, \mu m^3$.

eventually transitions into a second, slower relaxation regime (Fig. 9). At relatively large particle separations ($D/R > 0.2$), the cluster relaxation process is dominated by the capillary force, leading to rapid relaxation (i.e., the far-field case). However, in the second regime (i.e., the near-field case), lubrication forces begin to play a role, and the particles experience a resisting force from the thin liquid film between the particle surfaces, leading to much slower relaxation. To quantify this behavior, we define a characteristic relaxation time t_{cap} for the capillary relaxation mode (first regime) as the time required for 75%–80% of the relaxation to occur. Using the analytical model, we find $t_{cap} = 5.7 \, s$ (denoted by the red arrow in Fig. 9), which is only $\approx 9.5\%$ of the total relaxation time.

V. DISCUSSION

In this work, we investigate the dynamics of meniscus-bound two-particle clusters in extensional flow using an automated flow-based technique known as the Stokes trap. In all cases, the experimental results are complemented with analytical models. Our results show that during the breakup process, clusters begin by aligning along the principal axis of extension in planar extensional flow, followed by deformation of the liquid bridge and eventual breakup after the meniscus has stretched into a thin thread. The breakup time is affected by several forces and parameters, and the overall breakup process is well described by the analytical model. The interplay between the hydrodynamic drag force, capillary force, lubrication force, and interparticle HI is crucial in determining the breakup dynamics of these clusters. In general, the experimental data are in good agreement with results from the analytical model. Using the cluster breakup analytical model, we derive an expression to predict the critical capillary number Ca_{crit} in terms of the contact angle, initial particle separation, and the liquid bridge volume for cluster breakup in planar extensional flow. Cluster breakup time is also quantified as a function of Ca and V, and the dimensionless breakup time $t^*_{rupture}$ is plotted against Ca for various values of V. Our results show that larger Ca and smaller V values lead to smaller breakup times, whereas smaller Ca and larger V values result in longer breakup times. The relaxation dynamics of two-particle clusters were further characterized under zero-flow conditions. Our results show that cluster relaxation is a dual-mode process with the first, faster relaxation mode dominated by capillary forces, and a second, slower mode dominated by the lubrication force. An analytical model is developed for cluster relaxation, and good agreement is obtained between experiments and predictions from the analytical model.

The microscopic behavior of particle clusters is expected to directly influence the macroscopic properties of capillary suspensions. In this work, we focus on the case of two-particle clusters, which are the basic unit of capillary suspensions and hence provide a useful starting point for understanding the dynamic behavior of these systems. In practice, capillary suspensions are comprised of heterogeneous particle clusters containing a distribution of particle numbers ($N = 2, 3, 4, 5, \ldots$). In our experiments, we observe that

multiparticle clusters consisting of larger numbers of particles ($N > 2$) generally break up in a stepwise fashion until a two-particle doublet remains and is (itself) eventually broken up in flow. For these reasons, the determination of a critical capillary number Ca_{crit} for the case of two-particle cluster breakup in extensional flow provides fundamentally new and useful insights into the processing conditions at which capillary suspensions can be mixed without breaking liquid bridges, thus informing industrial operations by understanding the micromechanics of particle clusters.

In extensional flow, bulk stress in a capillary suspension is expected to rise as the accumulated fluid strain increases and liquid bridges are stretched, at least until the liquid bridge connections are broken. Following cluster breakup, a decrease in the bulk stress is expected as the liquid bridges can no longer resist deformation, and individual, nonconnected particles begin to move affinely with the flow. From this view, our work will help to inform the macroscopic properties and processing conditions of capillary suspensions to either promote or avoid breakup. Nevertheless, the macroscopic properties of a bulk capillary suspension will result from the cluster and volume-averaged behavior, and in practice, we expect a broad distribution of particle cluster sizes and cluster compositions ($N = 2, 3, 4, 5, \ldots$) in addition to a distribution of time scales at which the breakup behavior occurs due to different initial conditions (e.g., different initial orientation or cluster spatial conformation). For these reasons, the micromechanical behavior of particle clusters is not expected to map in a precise "one-to-one" manner to the bulk scale behavior of capillary suspensions. In an analogous manner, the coil-stretch transition of flexible polymers is predicted to occur at a critical dimensionless flow strength (Weissenberg number, $Wi = 0.5$) [50], which has been validated using single-molecule experiments [51–53]. However, polydispersity in polymer molecular weight leads to a "smearing out" of the sharpness of the transition when measured using bulk methods [54].

In dilute suspensions of fibers or flexible polymers (e.g., dumbbells), large viscous or elastic stresses can arise in extensional flows. Analogously, liquid bridge stretching is expected to give rise to increased stresses in capillary suspensions before breaking at a critical flow strength. Prior work focusing on breakup or deformation of Newtonian or non-Newtonian liquid drops was greatly informed by seminal work on individual droplets (as opposed to bulk experiments) from Taylor, Leal, and others [28–31]. A few bulk-scale experiments on liquid drop suspensions include work from Jansen *et al.* [55], who experimentally studied critical conditions for drop breakup in an emulsion undergoing shear flow. Results from this work showed an increased tendency for drop breakup in concentrated suspensions, which could be explained by a mean-field model treating the emulsion as a continuum with a larger effective viscosity than the suspending fluid. In 2010, Kaur and Leal [56] studied drop deformation and breakup in a concentrated suspension of refractive-index-matched PMMA particles in planar extensional flow. Here, the effect of many-body interactions on drop deformation was studied, revealing that the average deformation in the suspension increases with increasing

particle concentration due to an increased stress resulting from hydrodynamic interactions of particles. By drawing inspiration from these studies, when moving to more concentrated capillary suspensions, we might expect similar behavior in terms of an effective viscosity, critical flow strengths, and average stress in capillary suspensions. However, we caution that deriving more accurate relations between critical flow strength, cluster relaxation times, and suspension rheological properties will require rigorous quantitative analysis involving inter-cluster interactions and network formation, which are far beyond the scope of this study.

Overall, our work provides a new understanding of the dynamics and behavior of cluster breakup and relaxation for freely suspended particle clusters in extensional flow, which can be used to inform the processing of capillary suspensions for improved design of mixing operations.

ACKNOWLEDGMENTS

AUTHOR DECLARATIONS
Conflict of Interest

The authors have no conflicts to disclose.

DATA AVAILABILITY

The data that support the findings of this study are available from the corresponding author upon reasonable request.

REFERENCES

[1] Koos, E., "Capillary suspensions: Particle networks formed through the capillary force," Curr. Opin. Colloid Interface Sci. **19**, 575–584 (2014).

[2] Koos, E., and N. Willenbacher, "Capillary forces in suspension rheology," Science **331**, 897–900 (2011).

[3] Schneider, M., J. Maurath, S. B. Fischer, M. Weiß, N. Willenbacher, and E. Koos, "Suppressing crack formation in particulate systems by utilizing capillary forces," ACS Appl. Mater. Interfaces **9**, 11095–11105 (2017).

[4] Amoabeng, D., and S. S. Velankar, "Bulk soldering: Conductive polymer composites filled with copper particles and solder," Colloids Surf., A **553**, 624–632 (2018).

[5] Koos, E., J. Johannsmeier, L. Schwebler, and N. Willenbacher, "Tuning suspension rheology using capillary forces," Soft Matter **8**, 6620–6628 (2012).

[6] Hoffmann, S., E. Koos, and N. Willenbacher, "Using capillary bridges to tune stability and flow behavior of food suspensions," Food Hydrocolloids **40**, 44–52 (2014).

[7] Roh, S., D. P. Parekh, B. Bharti, S. D. Stoyanov, and O. D. Velev, "3D printing by multiphase silicone/water capillary inks," Adv. Mater. **29**, 1701554 (2017).

[8] Dittmann, J., E. Koos, and N. Willenbacher, "Ceramic capillary suspensions: Novel processing route for macroporous ceramic materials," J. Am. Ceram. Soc. **96**, 391–397 (2013).

[9] Studart, A. R., U. T. Gonzenbach, E. Tervoort, and L. J. Gauckler, "Processing routes to macroporous ceramics: A review," J. Am. Ceram. Soc. **89**, 1771–1789 (2006).

[10] Schneider, M., E. Koos, and N. Willenbacher, "Highly conductive, printable pastes from capillary suspensions," Sci. Rep. **6**, 31367 (2016).

[11] Yang, J., Z. Hu, H. Yan, and F. Niu, "Magnetorheological suspension with capillary network," J. Intell. Mater. Syst. Struct. **30**, 1850–1857 (2019).

[12] Van Kao, S., L. E. Nielsen, and C. T. Hill, "Rheology of concentrated suspensions of spheres. II. Suspensions agglomerated by an immiscible second liquid," J. Colloid Interface Sci. **53**, 367–373 (1975).

[13] Hauf, K., and E. Koos, "Structure of capillary suspensions and their versatile applications in the creation of smart materials," MRS Commun. **8**, 332–342 (2018).

[14] Bossler, F., L. Weyrauch, R. Schmidt, and E. Koos, "Influence of mixing conditions on the rheological properties and structure of capillary suspensions," Colloids Surf., A **518**, 85–97 (2017).

[15] D. McFarlane, J. S., and D. Tabor, "Adhesion of solids and the effect of surface films," Proc. R. Soc. London, Ser. A **202**, 224–243 (1950).

[16] Mason, G., and W. Clark, "Liquid bridges between spheres," Chem. Eng. Sci. **20**, 859–866 (1965).

[17] Willett, C. D., M. J. Adams, S. A. Johnson, and J. P. Seville, "Capillary bridges between two spherical bodies," Langmuir **16**, 9396–9405 (2000).

[18] Pitois, O., P. Moucheront, and X. Chateau, "Liquid bridge between two moving spheres: An experimental study of viscosity effects," J. Colloid Interface Sci. **231**, 26–31 (2000).

[19] Bozkurt, M., D. Fratta, and W. Likos, "Capillary forces between equally sized moving glass beads: An experimental study," Can. Geotech. J. **54**, 1300–1309 (2017).

[20] Lu, N., and W. J. Likos, *Unsaturated Soil Mechanics* (Wiley, Hoboken, New Jersey, 2004).

[21] Fisher, R., "On the capillary forces in an ideal soil; correction of formulae given by W. B. Haines," J. Agric. Sci. **16**, 492–505 (1926).

[22] Derjaguin, B., "Untersuchungen ueber die reibung und adhaesion, IV: Theorie des anhaftens kleiner teilchen," Kolloid Z. **69**, 155–164 (1934).

[23] Israelachvili, J. N., "Surface forces," in *The Handbook of Surface Imaging and Visualization* (CRC, Boca Raton, FL, 2022), pp. 793–816.

[24] Rabinovich, Y. I., M. S. Esayanur, and B. M. Moudgil, "Capillary forces between two spheres with a fixed volume liquid bridge: Theory and experiment," Langmuir **21**, 10992–10997 (2005).

[25] Butt, H.-J., and M. Kappl, "Normal capillary forces," Adv. Colloid Interface Sci. **146**, 48–60 (2009).

[26] Lian, G., C. Thornton, and M. J. Adams, "A theoretical study of the liquid bridge forces between two rigid spherical bodies," J. Colloid Interface Sci. **161**, 138–147 (1993).

[27] Maugis, D., "Adherence of elastomers: Fracture mechanics aspects," J. Adhes. Sci. Technol. **1**, 105–134 (1987).

[28] Taylor, G. I., "The formation of emulsions in definable fields of flow," Proc. Roy. Soc. Lond., Ser. A **146**, 501–523 (1934).

[29] Grace, H. P., "Dispersion phenomena in high viscosity immiscible fluid systems and application of static mixers as dispersion devices in such systems," Chem. Eng. Commun. **14**, 225–277 (1982).

[30] Bentley, B., and L. G. Leal, "An experimental investigation of drop deformation and breakup in steady, two-dimensional linear flows," J. Fluid Mech. **167**, 241–283 (1986).

[31] Stone, H. A., and L. G. Leal, "Relaxation and breakup of an initially extended drop in an otherwise quiescent fluid," J. Fluid Mech. **198**, 399–427 (1989).

[32] Shenoy, A., C. V. Rao, and C. M. Schroeder, "Stokes trap for multiplexed particle manipulation and assembly using fluidics," Proc. Natl. Acad. Sci. U.S.A. **113**, 3976–3981 (2016).

[33] Kumar, D., A. Shenoy, S. Li, and C. M. Schroeder, "Orientation control and nonlinear trajectory tracking of colloidal particles using microfluidics," Phys. Rev. Fluids **4**, 114203 (2019).

[34] Shenoy, A., D. Kumar, S. Hilgenfeldt, and C. M. Schroeder, "Flow topology during multiplexed particle manipulation using a stokes trap," Phys. Rev. Appl. **12**, 054010 (2019).

[35] Kumar, D., A. Shenoy, J. Deutsch, and C. M. Schroeder, "Automation and flow control for particle manipulation," Curr. Opin. Chem. Eng. **29**, 1–8 (2020).

[36] Tu, M. Q., H. V. Nguyen, E. Foley, M. I. Jacobs, and C. M. Schroeder, "3D manipulation and dynamics of soft materials in 3D flows," J. Rheol. **67**, 877–890 (2023).

[37] Dinic, J., Y. Zhang, L. N. Jimenez, and V. Sharma, "Extensional relaxation times of dilute, aqueous polymer solutions," ACS Macro Lett. **4**, 804–808 (2015).

[38] Dinic, J., M. Biagioli, and V. Sharma, "Pinch-off dynamics and extensional relaxation times of intrinsically semi-dilute polymer solutions characterized by dripping-onto-substrate rheometry," J. Polym. Sci. Part B: Polym. Phys. **55**, 1692–1704 (2017).

[39] Dinic, J., L. N. Jimenez, and V. Sharma, "Pinch-off dynamics and dripping-onto-substrate (DoS) rheometry of complex fluids," Lab Chip **17**, 460–473 (2017).

[40] Martínez Narváez, C. D., J. Dinic, X. Lu, C. Wang, R. Rock, H. Sun, and V. Sharma, "Rheology and pinching dynamics of associative polysaccharide solutions," Macromolecules **54**, 6372–6388 (2021).

[41] Lopez, R., J. Vaswani, D. T. Butler, J. McCarthy, and S. S. Velankar, "Low viscosity liquid bridges: Stretching of liquid bridges immersed in a higher viscosity liquid," JCIS Open **9**, 100079 (2023).

[42] Lian, G., and J. Seville, "The capillary bridge between two spheres: New closed-form equations in a two century old problem," Adv. Colloid Interface Sci. **227**, 53–62 (2016).

[43] Graham, M. D., *Microhydrodynamics, Brownian Motion, and Complex Fluids* (Cambridge University, Cambridge, 2018).

[44] Vincent, L., and P. Soille, "Watersheds in digital spaces: An efficient algorithm based on immersion simulations," IEEE Trans. Pattern Anal. Mach. Intell. **13**, 583–598 (1991).

[45] Preim, B., and C. P. Botha, *Visual Computing for Medicine: Theory, Algorithms, and Applications* (Newnes, San Francisco, CA, 2013).

[46] Kim, S., and S. J. Karrila, *Microhydrodynamics: Principles and Selected Applications* (Butterworth-Heinemann, Boston, MA, 1991).

[47] Koura, K., and H. Matsumoto, "Variable soft sphere molecular model for inverse-power-law or Lennard-Jones potential," Phys. Fluids. A **3**, 2459–2465 (1991).

[48] Rabani, E., and S. Egorov, "Interactions between passivated nanoparticles in solutions: Beyond the continuum model," J. Chem. Phys. **115**, 3437–3440 (2001).

[49] Liebetreu, M., and C. N. Likos, "Cluster prevalence in concentrated ring-chain mixtures under shear," Soft Matter **16**, 8710–8719 (2020).

[50] De Gennes, P., "Coil-stretch transition of dilute flexible polymers under ultrahigh velocity gradients," J. Chem. Phys. **60**, 5030–5042 (1974).

[51] Schroeder, C. M., H. P. Babcock, E. S. Shaqfeh, and S. Chu, "Observation of polymer conformation hysteresis in extensional flow," Science **301**, 1515–1519 (2003).

[52] Schroeder, C. M., E. S. Shaqfeh, and S. Chu, "Effect of hydrodynamic interactions on DNA dynamics in extensional flow: Simulation and single molecule experiment," Macromolecules **37**, 9242–9256 (2004).

[53] Schroeder, C. M., "Single polymer dynamics for molecular rheology," J. Rheol. **62**, 371–403 (2018).

[54] Fuller, G., and L. Leal, "Flow birefringence of dilute polymer solutions in two-dimensional flows," Rheol. Acta **19**, 580–600 (1980).

[55] Jansen, K., W. Agterof, and J. Mellema, "Droplet breakup in concentrated emulsions," J. Rheol. **45**, 227–236 (2001).

[56] Kaur, S., and L. G. Leal, "Drop deformation and break-up in concentrated suspensions," J. Rheol. **54**, 981–1008 (2010).

[57] See the supplementary material online for information on meniscus volume determination, interfacial tension measurements, particle surface roughness measurements, and mensicus fluid extensional viscosity.

05 April 2024 14:23:45